GeoScienceWorld
Lithosphere
Volume 2022, Article ID 2097990, 16 pages
https://doi.org/10.2113/2022/2097990

Lithosphere

Research Article

Combined Effect of Contact Area, Aperture Variation, and Fracture Connectivity on Fluid Flow through Three-Dimensional Rock Fracture Networks

Na Huang,[1,2] **Yubao Zhang**,[1] **Qian Yin**,[2] **Yujing Jiang**,[3] **and Richeng Liu**[2]

[1]*Key Laboratory of Mining Disaster Prevention and Control, Shandong University of Science and Technology, Qingdao 266590, China*
[2]*State Key Laboratory for Geomechanics and Deep Underground Engineering, China University of Mining and Technology, Xuzhou 221116, China*
[3]*School of Engineering, Nagasaki University, 1-14 Bunkyo-machi, 8528521 Nagasaki, Japan*

Correspondence should be addressed to Yubao Zhang; yubao.zhang@sdust.edu.cn

Received 9 March 2022; Accepted 25 May 2022; Published 6 June 2022

Academic Editor: Jean Borgomano

In order to investigate the combined effect of contact area, aperture variation, and fracture connectivity on the fluid flow through a fractured medium, a series of flow simulations were implemented on two types of three-dimensional discrete fracture network (3D DFN) models constituting fractures having spatially variable apertures and parallel plates, respectively. The flow tortuosity within the 3D DFN models was examined by changing the density, aperture distribution, and closure of fractures. The results show that compared with the 3D DFN models constituting parallel plates, the model with variable apertures provides more pronounced 3D preferential flow pathways. At the individual fracture scale, the preferential flow pathways mostly converge within the void spaces of large aperture, and at the network scale, they are located in the most transmissive fractures within the connected networks. The permeability of 3D DFNs depends not only on the contact area and aperture variation within individual fractures but also on the fracture connectivity and the contact at fracture intersections within the fracture network. Increasing the fracture connectivity tends to enhance the permeability, while increasing the contact at fracture intersections would significantly reduce the permeability. A correlation between the equivalent permeability of 3D DFNs constituting fractures with spatially variable apertures and parallel plates is proposed incorporating the effect of network-scale topology. A tortuosity factor for 3D DFNs is defined based on the proposed model, and it can account for two competing effects when the model is upscaled from individual fracture to fracture network: the permeability reduction induced by contact obstacles at fracture intersections and permeability enhancement induced by increasing the fracture connectivity.

1. Introduction

For crystalline rock masses with low matrix permeability, rock fractures are generally considered to be the main flow channels for fluids or solutes. Fracture-dominated flows have been a subject of interest in various fields of underground engineering, particularly within the energy sector such as development of geothermal and oil/gas reservoirs [1–4]. Natural fractured media show a significant geometrical complexity, which is induced by the surface roughness of single fractures and their arrangements in complex systems [5–9]. Precise modeling of geometries of both individual fracture and fracture network is a prerequisite to accurately predict the flow behaviors of fractured media. To mimic the geometrical properties of a natural fractured rock mass, the 3D discrete fracture network (DFN) model has been developed, in which each fracture is described by an individual plate with different sizes, apertures, locations, and orientations [10, 11]. As a result, contributions of each single fracture to the total flows of the network can be accounted for explicitly. However, in many previous studies, the fractures in 3D DFN models are frequently represented by

smooth parallel plates, despite the fact that the natural rock fractures have heterogeneous apertures induced by rough fracture walls. This simplification may introduce errors in predicting the permeability of fractures and flow pathways in them. Therefore, the DFNs constituting parallel plates require further improvement of the heterogeneous apertures to reveal the reality of the flow process in rock fracture networks [12–16].

In the 3D DFN models, the basic geometric object is the single fracture. The single rock fracture is typically characterized by two rough surfaces in partial contacts [17–22]. When fluid passes through such fractures, it mainly flows preferentially through large aperture channels. This phenomenon of preferential flow pathways is well known as channeling flow [23–27]. To model this flow process successfully, the tortuosity induced by both contact obstacles and aperture variations should be taken into account. Many previous researches focused on quantifying the influence of contacts and aperture variations on the permeability of single fractures [24, 28, 29]. The results show that depending on how the contact areas and void spaces within fractures are distributed, the permeability of rough-walled fractures can be either larger or smaller than that of fractures with the same average aperture, in which the cases of reduction are more frequent than the ones of augmenting [30–34]. The relationship between the permeability of the rough-walled fracture and the parallel plate model has been proposed by introducing different forms of tortuosity factors as a function of contact ratio, joint roughness coefficient (JRC), standard deviation of aperture distribution, etc. [35–39].

The fluid flow behavior in single fractures is affected not only by fracture geometry but also by stresses and resultant deformation of fractures [40–49]. When a fracture is subjected to normal or shear stress, its aperture may decrease because of closure induced by normal stress or increase because of dilation induced by shear stress. The variation of fracture aperture will further affect its hydraulic characteristics [50–53]. At moderate compressive stress levels, the changes of aperture during fracture closure can cause as much as three orders of magnitude change in permeability [54]. The deviation of flow characteristics of rough-walled rock fractures from that of the smooth parallel plates increases with the closing of fractures.

When the flow modeling is upscaled from within the single fractures to the fracture networks, fluids not only select the flow pathway of least resistance within the single fractures but also select the most transmissive fractures within the networks, which gives rise to the significant coupling effect of heterogeneous aperture distributions and network topology. The fracture network topology determines the model connectivity providing some potential flow pathways, and whether these potential flow pathways are available or not is further determined by the aperture distribution within the single fractures [55]. Numerous laboratory tests [13, 56], computational simulations [57, 58], and field studies [59, 60] of fluid flows in the rock fracture networks have demonstrated that the DFN model characterized by heterogeneous apertures could give more accurate permeability estimation than the model with parallel plates. Jing et al. [56] quantified that the permeability estimation based on the DFN model characterized by heterogeneous apertures provides fewer errors of 6.5% than that with the parallel plates. However, to date, studies focusing on the flow tortuosity induced by both the topology of fracture networks and the aperture variations in individual fractures for 3D DFNs are still few. A direct linking between the permeability of 3D DFN models constituting fractures with spatially variable apertures and parallel plates is still lacking.

The objective of the present study is to reveal the combined effect of contact areas, aperture variation, and fracture connectivity on the flow properties of 3D fracture networks. Two kinds of 3D DFN models constituting fractures with spatially variable apertures and the models having the same fracture topology but uniform aperture were generated. The flow behaviors through these DFN models were investigated by systematically varying the fracture density, aperture distribution, and fracture closure. A correction between the permeability of the two types of DFN models was proposed considering the influences of the contact area, aperture variations, and the topological properties of the 3D DFNs.

2. Theoretical Backgrounds

In early studies, the single fracture is usually simplified as a smooth parallel plate model having a fixed separation distance [61]. Laminar flow through this model obeys the cubic law, written as

$$Q = -\frac{\rho g b_h^3}{12\mu} w \frac{\partial h}{\partial x}, \tag{1}$$

where Q represents the flow rate, b_h represents the hydraulic aperture that equals to the mechanical aperture b (i.e., the perpendicular distance between two parallel plates), w represents the fracture width, μ represents the dynamic viscosity, ρ represents the fluid density, and h represents the hydraulic head. However, a natural rough-walled rock fracture usually has spatially variable apertures; thus, the assumption of parallel plates is obviously oversimplified. The Reynolds equation provides an approximate solution for flow through rough-walled rock fractures by dividing the voids between the upper and lower surfaces of the fracture into many connected parallel plates and assuming that the cubic law is valid locally within these small parallel plates. The Reynolds equation that is also recognized as the local cubic law is written as [62]

$$\frac{\partial}{\partial x}\left(\frac{\rho g b^3(x,y)}{12\mu}\frac{\partial h}{\partial x}\right) + \frac{\partial}{\partial y}\left(\frac{\rho g b^3(x,y)}{12\mu}\frac{\partial h}{\partial y}\right) = 0. \tag{2}$$

In Equation (2), $b(x, y)$ is usually set as spatially variable values to account for aperture distribution within natural rough fractures. Due to the tortuosity induced by the heterogeneity of void spaces and contacts between fracture walls, the hydraulic aperture of rough fractures cannot be directly geometrically measured. Its magnitude can be

back-calculated based on laboratory tests or bore-hole pump tests in the field [63, 64]. Zimmerman and Bodvarsson [65] proposed the following equation to estimate the hydraulic aperture:

$$b_h^3 = \langle b \rangle^3 \left[1 - 1.5 \left(\frac{s}{\langle b \rangle} \right)^2 \right], \tag{3}$$

where $<b>$ is the arithmetic mean of apertures and s is the standard deviation of apertures. Equation (3) implies that b_h becomes much smaller than $<b>$ with the increasing surface roughness.

When the two walls of the fracture are sufficiently close to each other, they would touch resulting in contact points with zero aperture. Equation (2) would break down at these contact points; thus, the contact regions and the void spaces should be treated separately in the flow calculations [66]. The parallel plate model with regularly distributed contact regions has been proposed to solely investigate the influence of contact areas on the permeability, without considering the variations of apertures [67]. Walsh [68] assumed circular cylindrical obstacles as the contacts between the parallel plates and derived the following expression using the Maxwell effective medium approach:

$$b_h^3 = b_n^3 \frac{1 - c}{1 + c}, \tag{4}$$

where b_n represents the separation distance of the parallel plates and c represents the contact ratio between total contact areas and apparent areas of the entire fracture plane. Equation (4) indicates that the hydraulic aperture decreases as the contact ratio increases. Later, Equation (4) is extended to the following expression for the elliptical-shaped obstacles [69]:

$$b_h^3 = b_n^3 \frac{1 - \beta c}{1 + \beta c}, \tag{5}$$

where $\beta = (1 + \alpha)^2/4\alpha$ and α represents the aspect ratio that is equal to the ratio of the minor to the major axis of the ellipse. Considering the difficulty in determining α for irregularly shaped contact barriers of natural rough-walled fractures, the factor (1-2c) proposed by Kirkpatrick [70] is applied to account for the effect of irregularly shaped obstacles. Combined with Equation (3), the following expression is obtained to calculate the hydraulic aperture of single fractures considering the influences of both aperture variations and contact obstacles [65]:

$$b_h^3 = \langle b \rangle^3 \left[1 - 1.5 \left(\frac{s}{\langle b \rangle} \right)^2 \right] (1 - 2c). \tag{6}$$

The equivalent permeability K of single rock fractures is defined as [37, 71]

$$K = \frac{Q\mu}{A\rho g \partial h/\partial x}, \tag{7}$$

where A represents the cross area of rock fracture. Since the equivalent permeability is proportional to the flow rate and also proportional to the cube of aperture, Equation (6) can be rewritten as

$$K = K_0 \left[1 - 1.5 \left(\frac{s}{\langle b \rangle} \right)^2 \right] (1 - 2c), \tag{8}$$

where K_0 is the equivalent permeability of fractures having an identical mean aperture.

3. Models and Methods

3.1. Model Generation. Since the natural fracture networks have complex geometrical topology, it is usually difficult to get an exhaustive description of the fracture properties such as fracture sizes, orientations, and positions. The stochastic DFN modeling approach can address this issue of uncertainty by generating the fracture networks with the fracture properties following given probability distributions [72, 73]. In this study, fractures are represented by circular disks having randomly distributed locations and orientations in the cubic domain of size L, which means that no position or orientation is favored within the domain. The fracture size l corresponding to the disk diameter is modeled by a power law distribution in the following form:

$$n(l) = \alpha \cdot l^{-a}, \tag{9}$$

where α represents the proportionality coefficient, $n(l) \cdot dl$ represents the number of fractures with the size varying in $[l, l + dl]$, and a represents the power law exponent varying in 2.0~4.5 [55]. The relative proportion of long and short fractures in the model is determined by the magnitude of a, in which a smaller value would generate a set of longer fractures, and vice versa. The measure of P_{32} defined as the total areas of fractures per unit volume is applied to represent fracture density. Four 3D DFN models with $P_{32} = 0.1$, 0.2, 0.3, and $0.4\,\mathrm{m^2/m^3}$ are generated as shown in Figure 1, and other detailed fracture properties of the model are tabulated in Table 1. Since this study focuses on the flow tortuosity induced by the aperture variability, the fluid behavior of denser DFNs is not considered to improve the computational efficiency. It should be noted that a single fracture model with $P_{32} = 0.1\,\mathrm{m^2/m^3}$ as shown in Figure 1(a) is specially generated, and this model will be regarded as a comparison to illustrate the fluid flow behavior through fracture networks.

3.2. Aperture Distributions. Large numbers of laboratory measurements have indicated that the aperture field of natural rock fractures is frequently distributed following the truncated Gaussian law [74, 75]. The frequency of truncated Gaussian law $f(b)$ can be written as

$$f(b) = \begin{cases} \dfrac{1}{s\sqrt{2\pi}} e^{-(b-\langle b \rangle)^2/2s^2}, & \text{if } b \geq 0, \\ 0, & \text{if } b < 0. \end{cases} \tag{10}$$

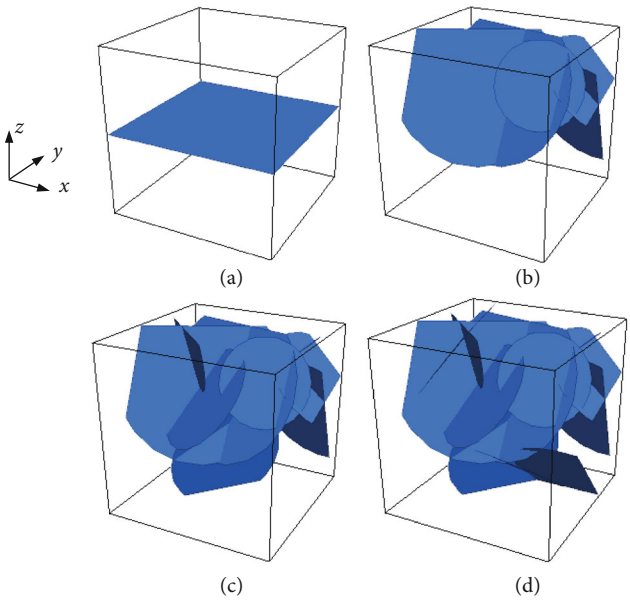

Figure 1: Generated 3D DFNs with different fracture densities: (a) $P_{32} = 0.1\ m^2/m^3$, (b) $P_{32} = 0.2\ m^2/m^3$, (c) $P_{32} = 0.3\ m^2/m^3$, and (d) $P_{32} = 0.4\ m^2/m^3$.

Table 1: Geometrical characteristics of the DFNs.

Parameter	Distribution	Value
Domain size (m)		$L = 20$
Positions	Uniform	
Orientations	Uniform	
Length (m)	Power law	$a = 2.5, 0.5 \le l/L \le 1$
Fracture density (m^2/m^3)		$P_{32} = 0.1$, 0.2, 0.3, and 0.4
Aperture (mm)	Gaussian distribution	$<b> = 1.35$ and 1.65, $s = 1.66$ and 1.96
Closure (mm)		$c_l = 0$, 0.2, 0.4, 0.6, 0.8, and 1.0

The normal stress applied to the rock fractures will induce the closure of two fracture walls, which reduces the apertures and increases the contact areas. This study generates four aperture distributions with different means and deviations as shown in Figure 2. For each aperture distribution, six fracture closures with $c_l = 0$, 0.2, 0.4, 0.6, 0.8, and 1.0 mm are considered, respectively. The aperture distribution under closure c_l is equal to the aperture at zero closure minus c_l, in which a small positive value is substituted for the negative value of the aperture to represent the contact. Two types of 3D DFN models are established, i.e., the DFN constituting fractures with heterogeneous apertures (denoted as DFN-H model) and the DFN constituting fractures with identical apertures (denoted as DFN-I model), to investigate the influence of the aperture heterogeneity on the fluid flow in fracture networks. The aperture field in the 3D DFN-H model follows the truncated Gaussian law. For comparison, the aperture of each fracture in the 3D DFN-I model is uniformly distributed, and its magnitude equals to the average aperture of the same fracture in the 3D DFN-H model.

3.3. Flow Simulation Methods. Fluid flow through each individual fracture in 3D DFNs is modeled by Equation (2). Considering that the flow domain of 3D DFNs consists of a number of fractures intersecting with each other, the flow model of individual fractures should be supplemented by the continuity equations on fracture intersections S_i to arrive at the overall flow of DFNs. The continuity equations on S_i are written as [10]

$$\begin{cases} h_{i,k} = h_i, \forall k \in F_i, \\ \sum_{k \in F_i} \mathbf{q}_{i,k} \mathbf{n}_{i,k} = 0, \end{cases} \tag{11}$$

where $h_{i,k}$ represents the trace of the hydraulic head on S_i in a fracture k, h_i represents the hydraulic head on S_i, F_i represents the fracture set intersecting on S_i, $\mathbf{q}_{i,k}$ represents the flow rate through S_i of the fracture k, and $\mathbf{n}_{i,k}$ represents the unit vector of S_i in the fracture k.

In this study, the density and viscosity of water at 10°C are utilized with $\rho = 9.997 \times 10^2\ kg/m^3$, $\mu = 1.307 \times 10^{-3}$ Pa·s, and $g = 9.807\ m/s$. Two fixed hydraulic head boundaries are applied on the opposite surfaces (Γ_{in} and Γ_{out}) of the DFN model, and other surfaces of the model are viewed as no flow boundaries, which are written as

$$\begin{cases} h = h_1, & \text{on } \Gamma_k \cap \Gamma_{in}, \\ h = h_2, & \text{on } \Gamma_k \cap \Gamma_{out}, \\ \mathbf{n} \nabla h = 0, & \text{on } \Gamma_k \setminus (\Gamma_{in} \cup \Gamma_{out}), \end{cases} \tag{12}$$

where Γ_k represents the border of the fracture k.

The fluid flow through 3D DFNs is solved by using the calculation procedure developed by the authors [76]. The 3D DFN models are constructed according to the given probability distributions of geometrical characteristics, in which the fractures isolated from the fracture clusters are removed to simplify the calculation. Then, the fractures in the model are meshed individually, imposing the constraints that the triangular grids are 2D in each fracture and the grid nodes match in the intersection between fractures. These constraints allow to easily implement the continuity conditions of Equations (11). Finally, the Galerkin scheme is applied to solve the flow equations combined with the continuity equations at fracture intersections. The details of the modeling and solution procedure are described in Huang et al. [76].

4. Results and Analysis

4.1. 3D Channeling Flow in DFNs. Figure 3 displays examples of aperture fields within the fracture networks displayed in Figure 1, in which apertures of 3D DFN-H models follow the truncated Gaussian law with $<b> = 1.35$ mm, $s = 1.66$ mm, and $c_l = 0$. The aperture distribution in the 3D DFN-H model displays strong heterogeneity due to the wide

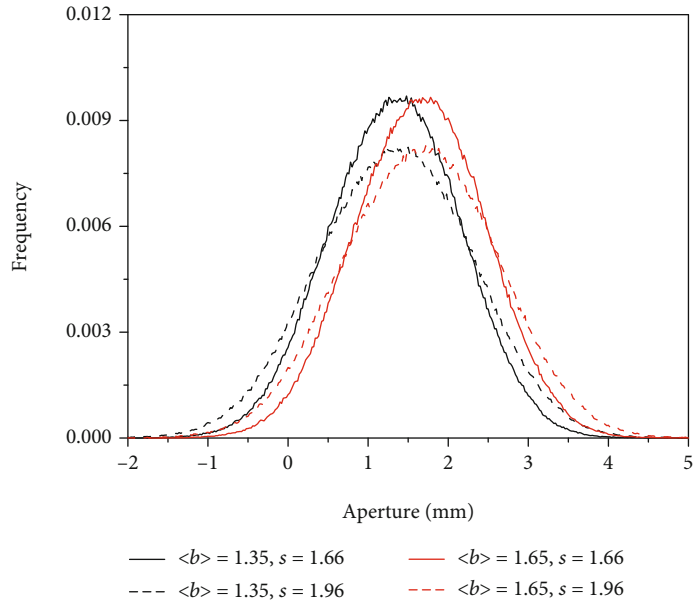

FIGURE 2: Aperture distributions with different means and deviations. The negative values are set to be a very small positive value in the calculation to represent the contacts between two fracture walls.

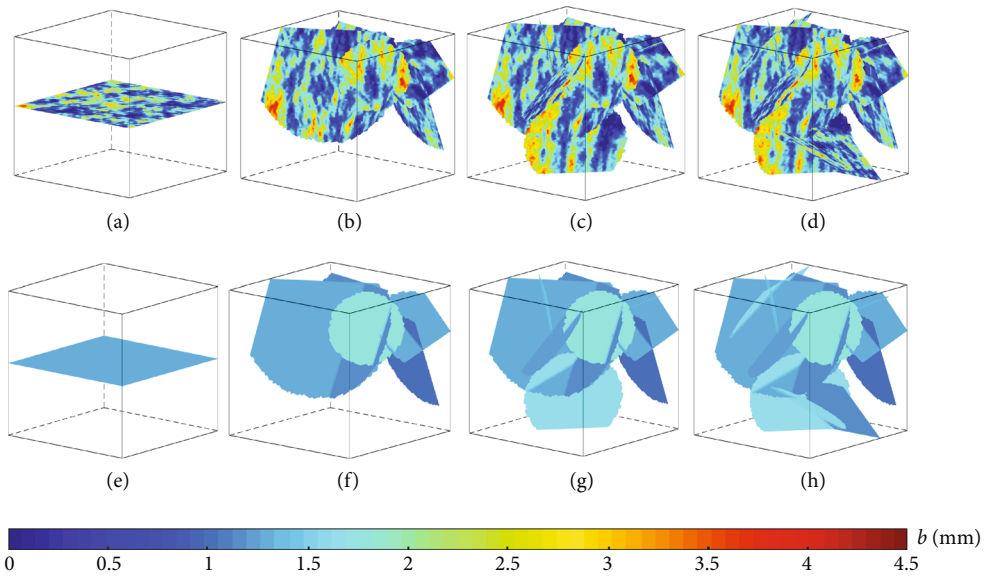

FIGURE 3: Aperture fields within 3D DFNs shown in Figure 1. The top side displays the DFN-H models in which the apertures follow the truncated Gaussian law with $<b> = 1.35$ mm, $s = 1.66$ mm, and $c_l = 0$. The bottom side displays the DFN-I models that are composed of parallel plates of identical mean aperture.

range of local apertures and large numbers of contacts. On the contrary, for the 3D DFN-I model, the apertures are uniform within each individual fracture but vary among different fracture planes. The resulting flow pathways in the aperture fields displayed in Figure 3 are illustrated in Figure 4. The color intensity in Figure 4 indicates the distribution of the ratio (F_l/Q) between the local flow rate (F_l) at each point and the total flow rate (Q) of whole fracture networks, reflecting the relative contribution of each point to total flows. The contribution of points with ratios smaller than 0.005 is assumed to be negligible.

Obvious localizations of colored channels are observed in Figures 4(a)–4(d), which indicates the development of significant preferential flows within the 3D DFN-H models. At the individual fracture scale, the main flow channels are concentrated in the void space of large apertures. At the network scale, the flow pathways are located in most transmissive fractures within the connected networks. The comparison of flow fields in Figures 4(b) and 4(d) indicates that main flow channels at both fracture and network scales change with increasing the fracture density. This is because the increment of fracture density would

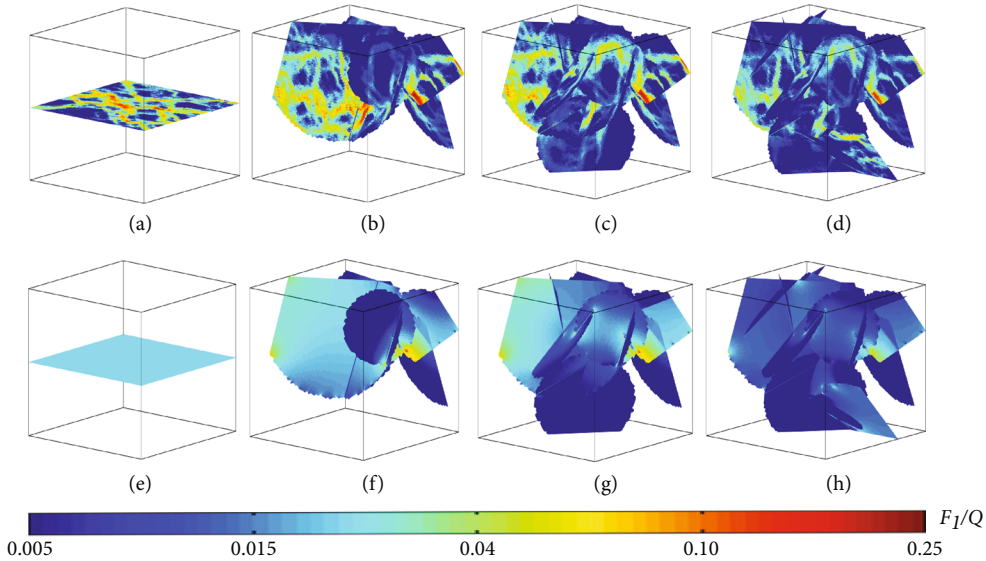

FIGURE 4: Fluid flows within the heterogeneous apertures (top) that follow the truncated Gaussian distribution with $<b> = 1.35$ mm, $s = 1.66$ mm, and $c_l = 0$, and the identical mean apertures (bottom).

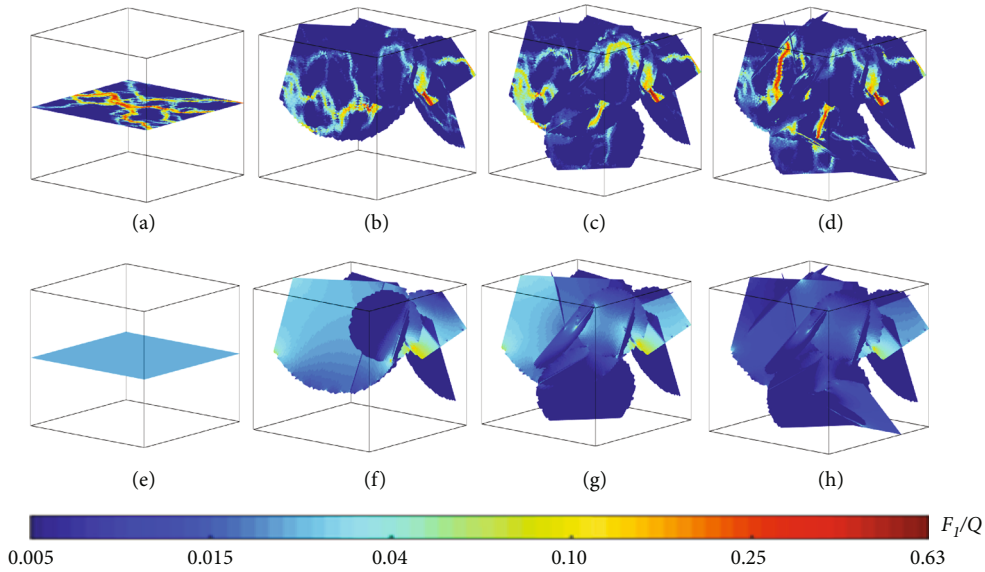

FIGURE 5: Fluid flows within the heterogeneous apertures (top) that follow the truncated Gaussian distribution with $<b> = 1.35$ mm, $s = 1.66$ mm, and $c_l = 1.0$ mm and the identical mean apertures (bottom).

essentially increase the number of connected fractures, thereby providing more potential flow pathways that allow the fluid to reselect. The flow rates within the single fracture of identical aperture are uniformly distributed (Figure 4(e)). However, the phenomenon of channeling flow is observed within the 3D DFN-I model as shown in Figures 4(f)–4(h), despite the fact that the flow channels are much less obvious than those within the DFN-H model. This phenomenon mainly arises from the stochastic fracture properties (i.e., the size, location, and orientation of fractures) and also from the aperture deviations between different fractures.

Figure 5 displays the fluid flow within the aperture fields having the same truncated Gaussian distribution as that in Figure 4, but an increasing fracture closure of $c_l = 1.0$ mm. The comparison of the flow fields in Figures 4 and 5 shows that flow channels in the model decrease with the increment of fracture closure owing to two factors: (1) the decrease in fracture aperture due to fracture closure and (2) the decrease in flow connectivity and increase in flow tortuosity as a result of the increasing contact areas. This phenomenon is similar to that observed in single rock fractures under the closure induced by stresses [26, 77].

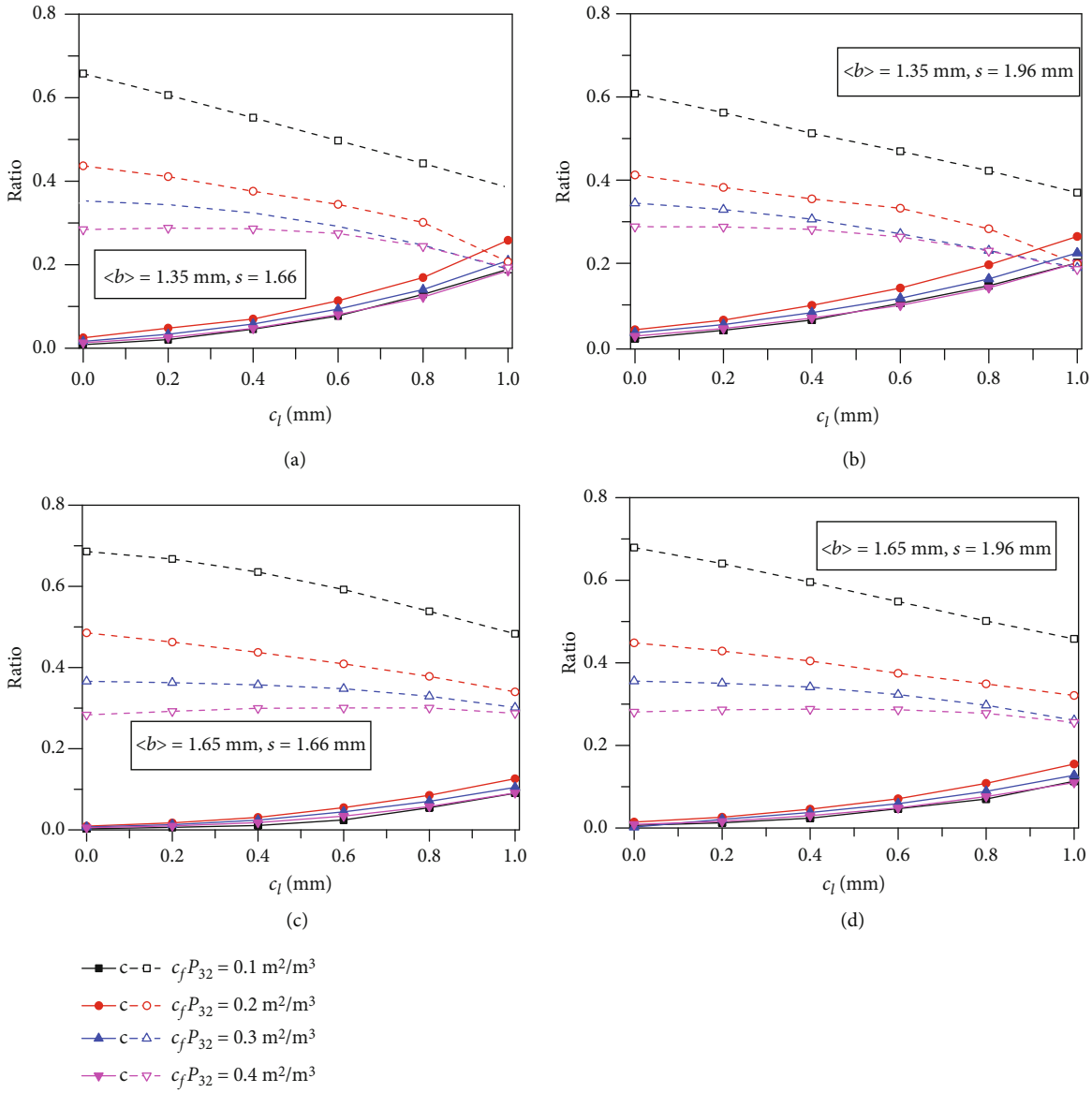

FIGURE 6: Variations in contact ratio (c) and flow area ratio (c_f) represented by the solid and dashed lines, respectively, during fracture closure.

Figure 6 illustrates the variations of contact ratio (c) and the flow area ratio (c_f, equaling to the ratio of areas of flow channels with $F_l/Q \geq 0.005$ to the apparent areas of all fractures) during the closure for 3D DFN-H models. For all cases, the contact ratio increases, and the flow area ratio decreases as the fracture closure increases, showing consistent results with the that obtained from Figures 4 and 5. The flow area ratios significantly decrease when increasing fracture density, while the change in contact ratios with fracture density is not so obvious. Depending on the fracture closure, fracture density, and aperture variation, contact areas within the 3D DFN-H models are approximately 0~25% of total fracture planes. Correspondingly, flow areas are approximately 70%~20% of total fracture planes, which are much smaller than the noncontact areas. The noncontact areas consist of flow areas and stagnant areas [26]. As the fracture density increases, the stagnant areas in the 3D DFN-H models significantly increase, indicating an increasingly obvious phenomenon of preferential flow.

4.2. Permeability. The variations in equivalent permeability with fracture density for the 3D DFN-H models under different fracture closures are displayed in Figure 7. Because the fractures in the 3D DFN-H model with $P_{32} = 0.2\,m^2/m^3$ less effectively contribute to the connectivity than the model with a single fracture that connects the inlet and outlet boundaries directly, the equivalent permeability firstly decreases as the fracture density increases from 0.1 to $0.2\,m^2/m^3$. Then, the equivalent permeability changes to increase with increasing fracture density, owing to more alternative flow pathways within the 3D DFN-H model with a larger fracture density. The equivalent

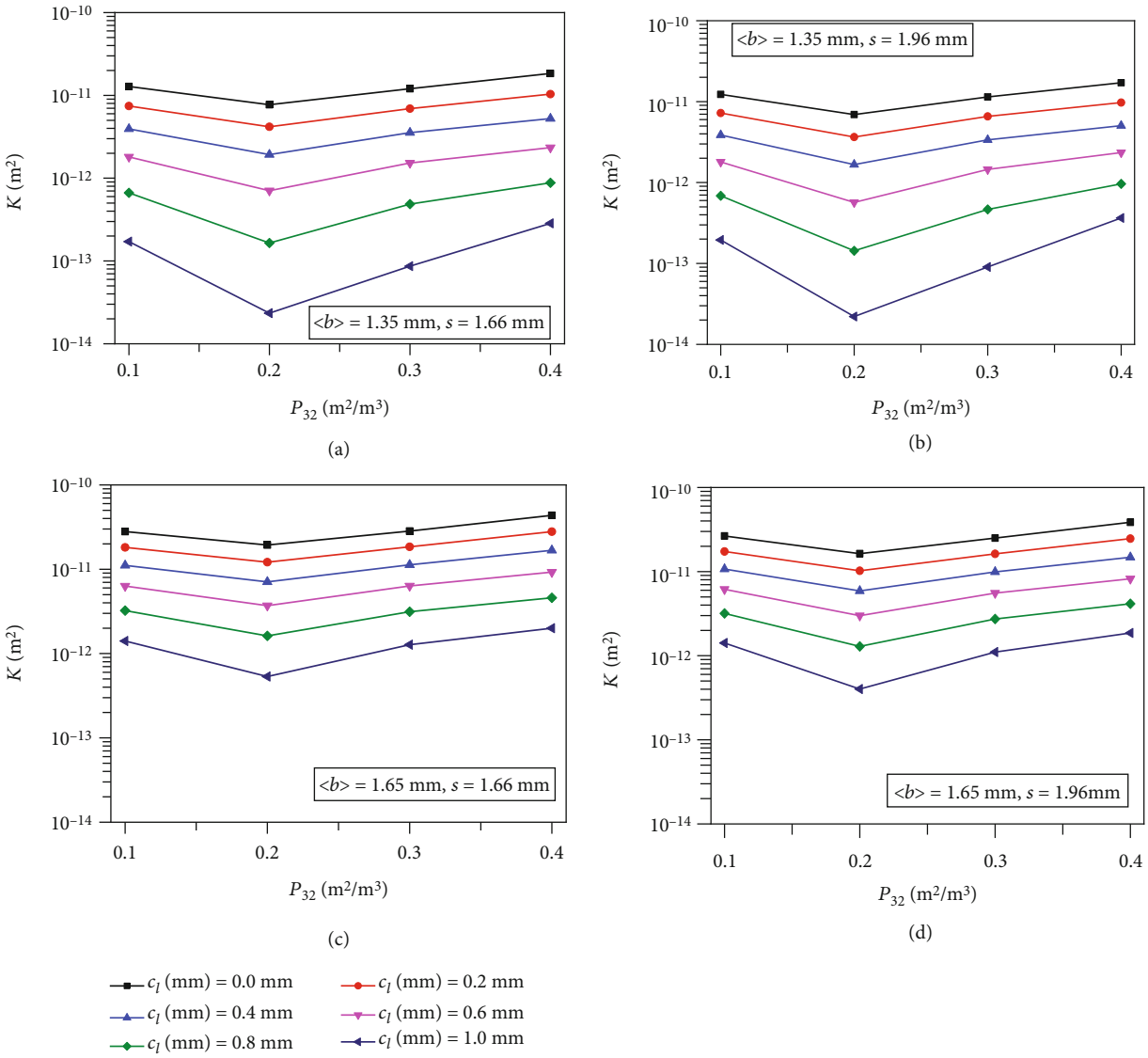

Figure 7: Variation in equivalent permeability with fracture density for 3D DFN-H models under different fracture closures.

permeability consistently decreases with increasing the fracture closure, in which the decrement is more obvious under a larger fracture closure.

The equivalent permeability ratio (K/K_0) between 3D DFN-H models and 3D DFN-I models is estimated, and its evolution during fracture closure is illustrated in Figure 8. For all cases, K/K_0 is less than 1.0, indicating that the equivalent permeability of fracture networks is systematically reduced by the variations in local apertures. K/K_0 decreases as the mean aperture decreases and/or the deviation of apertures increases. In addition, K/K_0 decreases with increasing the fracture closure. This reduction of the permeability ratio first comes from the influence of fracture closure-enhanced flow tortuosity at a single fracture scale. Besides, the decrease in apertures and/or increase in contact areas at fracture intersections as a result of fracture closure may break up the otherwise available flow pathways, thereby significantly reducing the permeability of 3D DFN-H models.

4.3. A New Correlation between K and K_0. Besides the factors such as the aperture variations and contact areas within single fractures, the fracture density and aperture distribution at fracture intersections also affect the permeability of 3D DFNs. Increasing the fracture density would increase the network connectivity, thereby providing more alternative flow pathways in the fracture network. However, whether the connected pathways are available or not for fluid flows would further depend on the fracture apertures. The apertures within a fracture plane are commonly correlatively distributed, which tends to easily generate at least one continuous flow pathway therein. But the aperture fields in different fracture planes are independent, which may result in closed areas at fracture intersections thus breaking up the flow pathways between fractures. Therefore, the following expression incorporating the factors of fracture connectivity and contact ratio at fracture intersections is proposed for 3D DFNs, written as

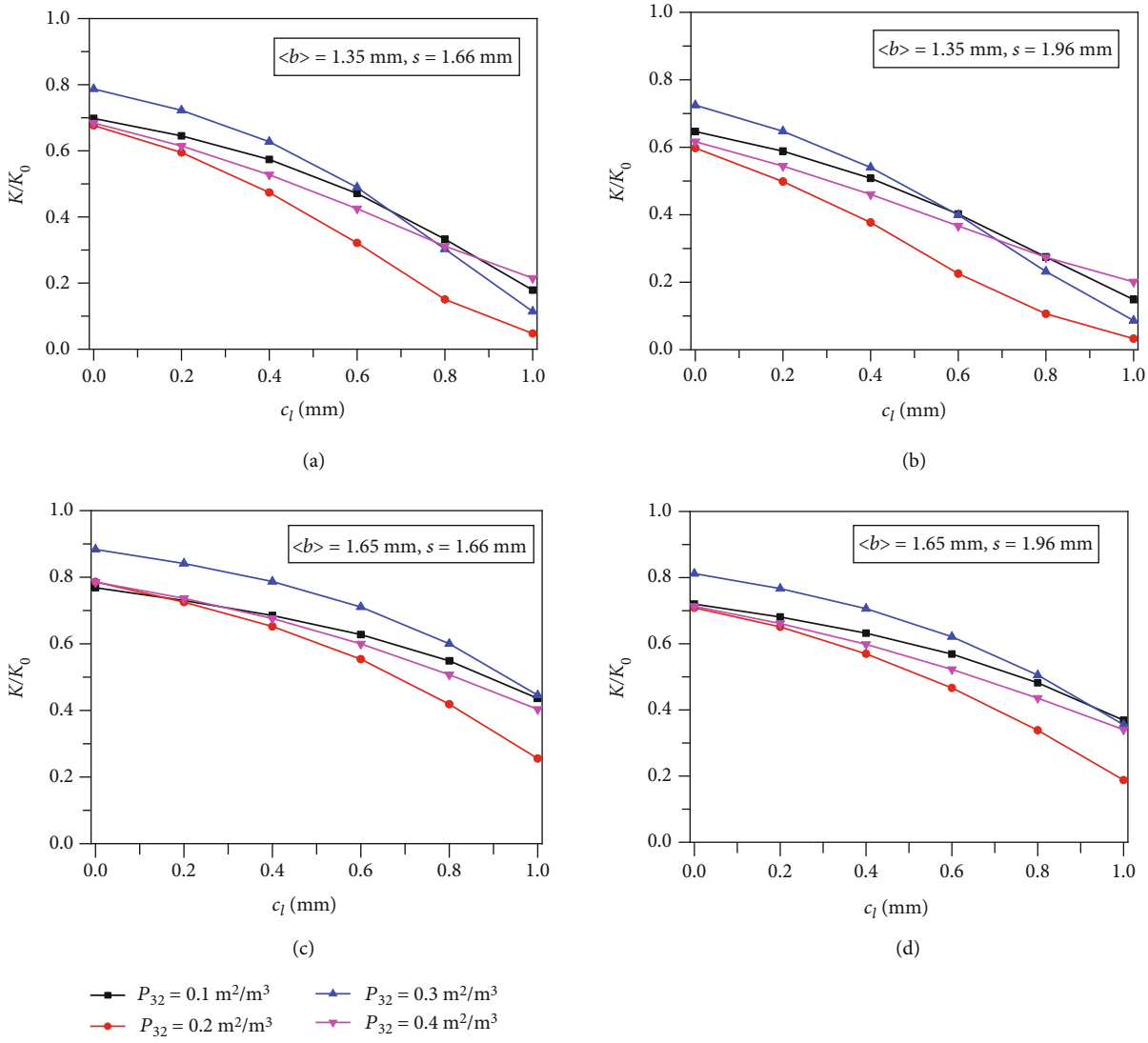

FIGURE 8: Variation in K/K_0 during fracture closure for models with different fracture densities and aperture distributions.

$$K = K_0\left[1 - 1.5\left(\frac{s}{\langle b\rangle}\right)^2\right](1-2c) \cdot \left[2 - \frac{2}{1+\mathrm{EXP}(L_{MI}P_{32}/4)}(1-2c_I)^2\right], \quad (13)$$

where L_{MI} is the mean length of fracture intersections defined as $L_{MI} = L_I/N_I$, in which L_I represents total fracture intersection length, N_I represents the number of fracture intersections, and c_I is the contact ratio at fracture intersections defined as the ratio between the number of zero-aperture nodes and total number of nodes at fracture intersections. In Equation (13), the expression with $L_{MI}P_{32}$ accounts for the effect of enhancement of permeability induced by the increase in the fracture connectivity, and the expression with $(1-2c_I)$ accounts for the effect of the reduction of permeability induced by the contacts at fracture intersections. For the single fracture with $L_{MI} = 0$ and $c_I = 0$, Equation (13) can be simplified as Equation (8). L_I, N_I, and L_{MI} for 3D DFNs with different densities are estimated. Both L_I and N_I increase with increasing fracture density as illustrated in Figure 9(a). L_{MI} displayed in Figure 9(b) decreases slightly as fracture density increases from 0.2 to 0.4 m^2/m^3.

Figure 10 displays the comparison of simulated equivalent permeability of the single fracture model ($P_{32} = 0.1\ m^2/m^3$) with the results predicted using Equation (13). Equation (13) could give a reasonable prediction of equivalent permeability for the single fractures under a small closure. As the fracture closure increases, the contact ratio c increases, and Equation (13) tends to overestimate the equivalent permeability of the single fracture model. This overestimation has also been reported by Gale et al. [78] and Yeo [39]. They suggested changing the constant of 2 before c in Equation (8) as 2.4 to reflect the strong impact of contact areas on the permeability by increasing the contact ratio. The simulated equivalent permeability of 3D DFN-H models ($P_{32} = 0.2\sim0.4\ m^2/m^3$) is compared to the results predicted using Equation (13) as illustrated in Figure 11. The two data

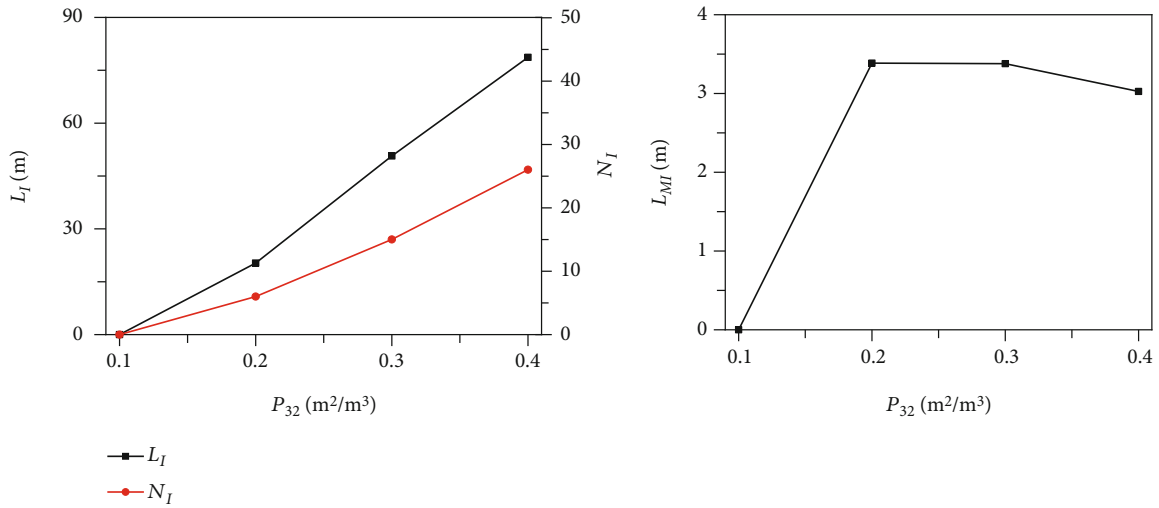

FIGURE 9: Variations in total length of intersections (L_I), total number of intersections (N_I), and mean length of intersections ($L_{MI} = L_I/N_I$) with fracture density.

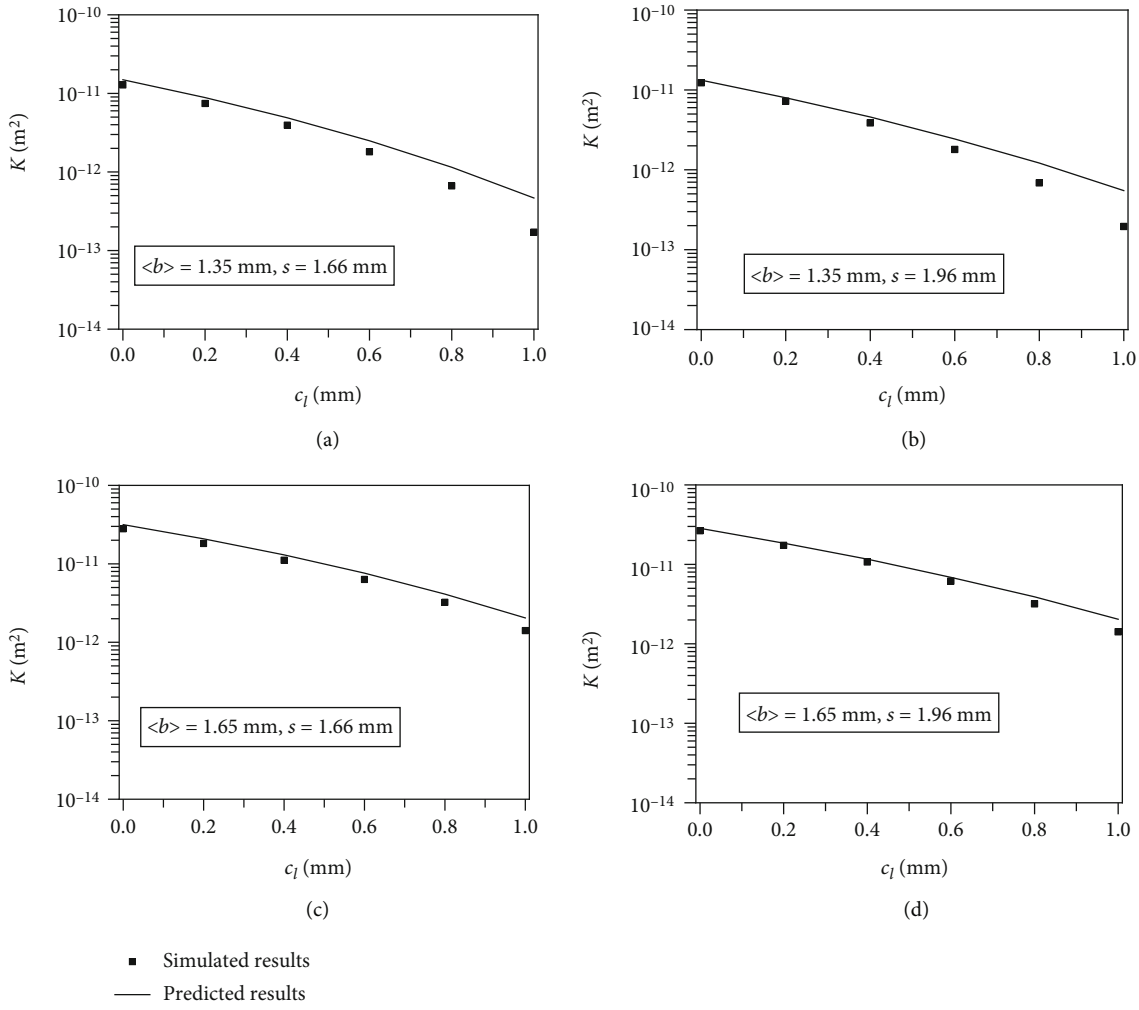

FIGURE 10: Comparisons of simulated equivalent permeability of the single fracture ($P_{32} = 0.1\ m^2/m^3$) with the result predicted using Equation (13).

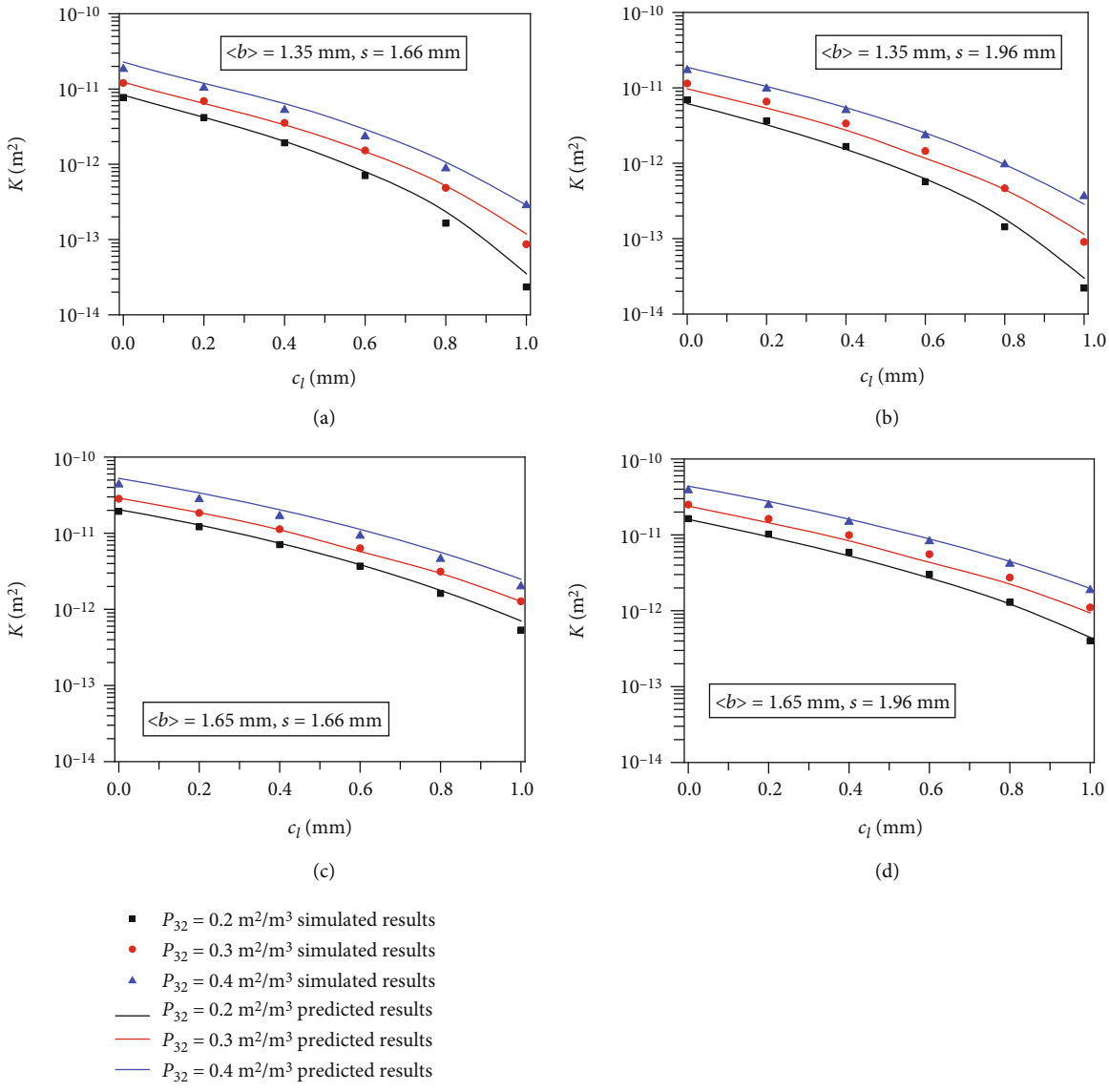

Figure 11: Comparisons of simulated equivalent permeability of 3D DFN-H models with that predicted using Equation (13).

sets agree well with each other in the closure range studied here, which indicates that Equation (13) can reasonably predict the effects of aperture variation and contact area on permeability of the 3D DFN-H models. Equation (13) is proposed based on the DFNs with random orientation and location of fractures. However, the natural fracture orientation may form clusters around some statistically preferred directions, which will influence the permeability of DFNs significantly and should be studied in future works.

To quantify the tortuosity induced by the complex geometry of void spaces and contact obstacles within fractures and topology of fracture networks, the tortuosity factors τ_1 and τ_2 are defined, written as

$$\tau_1 = \left[1 - 1.5\left(\frac{s}{\langle b\rangle}\right)^2\right](1-2c), \tag{14}$$

$$\begin{aligned}\tau_2 &= \left[1 - 1.5\left(\frac{s}{\langle b\rangle}\right)^2\right](1-2c)\\ &\quad\cdot\left[2 - \frac{2}{1+\mathrm{EXP}(L_{MI}P_{32}/4)}(1-2c_I)^2\right]\\ &= \tau_1\cdot\left[2 - \frac{2}{1+\mathrm{EXP}(L_{MI}P_{32}/4)}(1-2c_I)^2\right].\end{aligned} \tag{15}$$

Besides the factors of contact ratio and aperture variation at the fracture scale that are incorporated in τ_1, τ_2 can also account for the impact of fracture connectivity and contact ratio at fracture intersections on the fluid flow at the fracture network scale. The tortuosity of fluid flow through the 3D DFN-H models is evaluated using Equations (14) and (15), respectively. As shown in Figure 12, both τ_1 and τ_2 are always smaller than 1 and decrease monotonically with the fracture closure. For the single fracture model with

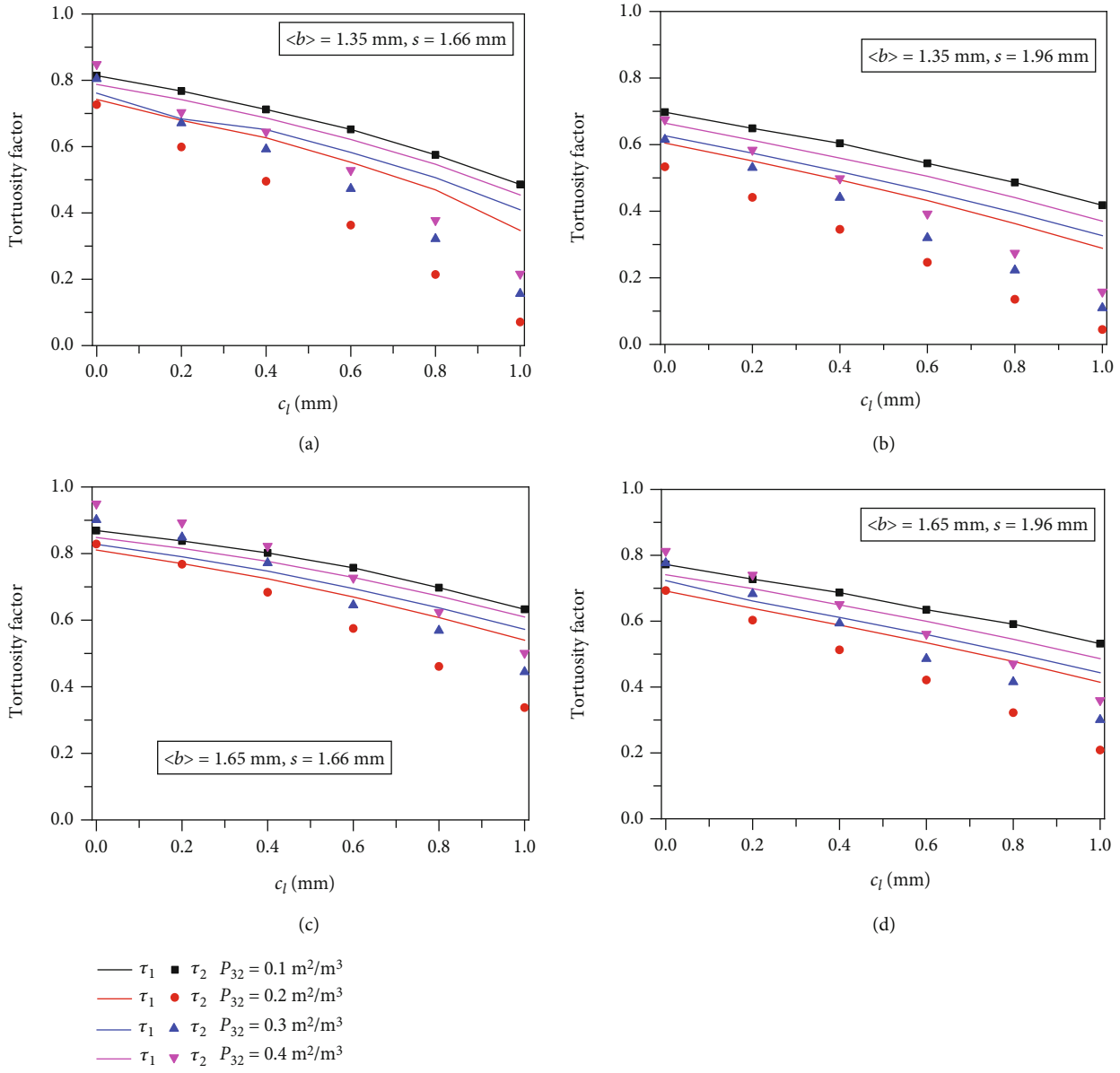

FIGURE 12: Variations in tortuous factors under different fracture closures. The solid line represents the tortuous factor τ_1, and the dot line represents the tortuous factor τ_2.

$P_{32} = 0.1\,m^2/m^3$, τ_1 and τ_2 have the same magnitude. For other cases with P_{32} varying from 0.2 to $0.4\,m^2/m^3$, τ_1 is slightly smaller than τ_2 at small fracture closure. However, as fracture closure increases, τ_1 becomes significantly larger than τ_2. The ratio of τ_1 to τ_2, written as $\alpha = \tau_1/\tau_2$, is estimated and illustrated in Figure 13. The value of α is a measure of two competing effects when the model is upscaled from individual fracture to fracture networks: the permeability reduction induced by contact obstacles at fracture intersections and permeability enhancement induced by increasing the fracture connectivity. The value less than 1.0 implies that permeability enhancement induced by increasing network connectivity is more remarkable than the reduction caused by the contact obstacles at fracture intersections. Conversely, a value larger than 1.0 indicates that the enhancement is less marked than the reduction. As shown in Figure 13, α varies from 0.8 to 6.5 and systematically increases with fracture closure except for the single fracture model with a constant $\alpha = 1$. Considering all DFN-H models displayed in Figure 13, the cases with $\alpha > 1$ are more frequent than the ones with $\alpha < 1$, which indicates that while increasing fracture connectivity tends to increase the number of potential flow pathways, the increased contact obstacles at fracture intersections with fracture closure further break up some of these flow pathways, thereby reducing the permeability. Since the fracture intersection is usually mechanically damaged [79, 80], the aperture of fracture intersections is usually larger than that of a single fracture. In this study, the fracture intersection

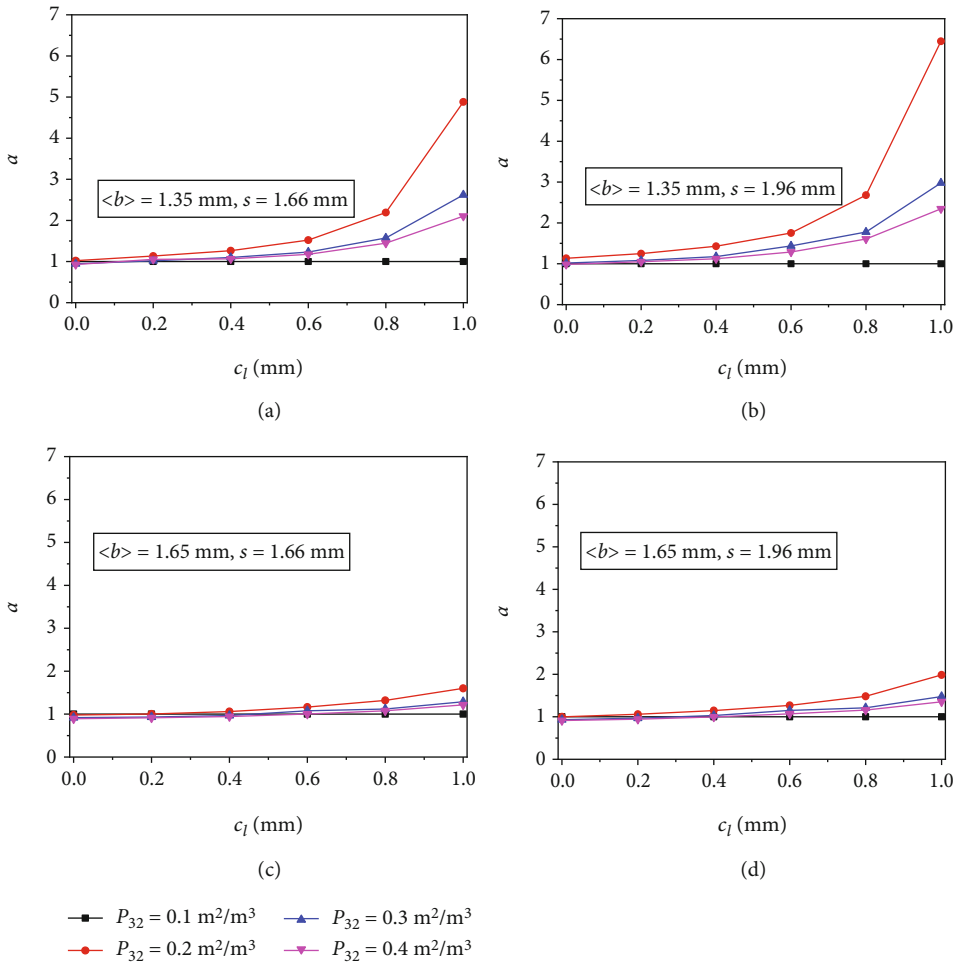

FIGURE 13: Variation in α during fracture closure for models with different fracture densities and aperture distributions.

has the same aperture as that of the two intersected fractures. In future works, the aperture of the fracture and fracture intersection will be assigned separately based on the field observation, and its influence on the permeability of 3D DFNs will be investigated.

5. Conclusions

In the present study, we have established a number of 3D DFNs to analyze the combined effect of contact area, aperture variation, and fracture connectivity on flow pattern and permeability of rock fracture networks. The fracture aperture within the models obeys the truncated Gaussian distribution and varies with the fracture closure. For comparisons, the fracture networks having the same fracture topology but uniform aperture were also generated. The flow behaviors through fracture networks were numerically investigated, and the roles of contact area, aperture variation, fracture density, and fracture intersection in the hydraulic properties of 3D DFNs were illustrated.

The results show that an obvious channeling effect of fluid flows is observed at both fracture and network scales of 3D DFNs, which is induced by the stochastic geometrical characteristics of single fractures (i.e., fracture size, orientation, location, and aperture) and aperture variations between different fractures. When the contact area increases from 0 to 25% of total fracture planes during fracture closure, the main flow area decreases from 70% to 20% of total fracture planes. The ratio of the equivalent permeability of 3D DFN models having spatially variable apertures to that having an identical mean aperture is less than 1.0, indicating that the permeability of fracture networks is systematically reduced by the variations in local apertures. This reduction of the permeability is controlled by the contact areas and aperture variation within each single fracture, as well as by the fracture connectivity and the contact at fracture intersections within the fracture network. A correlation between the equivalent permeability of 3D DFNs constituting fractures with spatially variable apertures and parallel plates is proposed as a function of parameters of single fractures (i.e., mean and deviation of aperture distributions and contact ratio) and fracture networks (i.e., contact ratio at fracture intersections, mean length of fracture intersections, and fracture density). This correlation is an extension of the expression for single fractures. A tortuosity factor for 3D DFNs is defined based on the proposed correction, and it can account for two competing effects when the model is upscaled from individual fracture to fracture network: the permeability

reduction induced by contact obstacles at fracture intersections and permeability enhancement induced by increasing the fracture connectivity.

Data Availability

The data used to support the findings of this study are included within the article.

Conflicts of Interest

The authors declare that they have no known competing financial interests or personal relationships that could have appeared to influence the work reported in this paper.

Acknowledgments

This study has been partially funded by the National Natural Science Foundation of China (No. 51909269), Key Laboratory of Mining Disaster Prevention and Control (No. MDPC201923), State Key Laboratory for Geomechanics and Deep Underground Engineering of China University of Mining and Technology (No. SKLGDUEK2102), and Major Basic Research Projects of Natural Science Foundation of Shandong Province (No. ZR2019ZD14). These supports are gratefully acknowledged.

References

[1] X. Cai and W. Liu, "Hydromechanical-coupled cohesive interface simulation of complex fracture network induced by hydrofracturing with low-viscosity supercritical CO_2," *Lithosphere*, vol. 2021, no. Special 1, article 6689981, 2021.

[2] A. Ghassemi, "A review of some rock mechanics issues in geothermal reservoir development," *Geotechnical and Geological Engineering*, vol. 30, no. 3, pp. 647–664, 2012.

[3] A. Orangi, N. R. Nagarajan, M. M. Honarpour, and J. J. Rosenzweig, "Unconventional Shale Oil and Gas-Condensate Reservoir Production, Impact of Rock, Fluid, and Hydraulic Fractures," in *SPE hydraulic fracturing technology conference*, Society of Petroleum Engineers, 2011.

[4] M. Vishkai and I. Gates, "On multistage hydraulic fracturing in tight gas reservoirs: Montney formation, Alberta, Canada," *Journal of Petroleum Science and Engineering*, vol. 174, pp. 1127–1141, 2019.

[5] T. Babadagli, X. Ren, and K. Develi, "Effects of fractal surface roughness and lithology on single and multiphase flow in a single fracture: an experimental investigation," *International Journal of Multiphase Flow*, vol. 68, pp. 40–58, 2015.

[6] S. Feng, H. Wang, Y. Cui et al., "Fractal discrete fracture network model for the analysis of radon migration in fractured media," *Computers and Geotechnics*, vol. 128, p. 103810, 2020.

[7] A. Jafari and T. Babadagli, "Estimation of equivalent fracture network permeability using fractal and statistical network properties," *Journal of Petroleum Science and Engineering*, vol. 92, pp. 110–123, 2012.

[8] J. Maillot, P. Davy, R. Le Goc, C. Darcel, and J. R. de Dreuzy, "Connectivity, permeability, and channeling in randomly distributed and kinematically defined discrete fracture network models," *Water Resources Research*, vol. 52, no. 11, pp. 8526–8545, 2016.

[9] J. Qian, H. Zhan, W. Zhao, and F. Sun, "Experimental study of turbulent unconfined groundwater flow in a single fracture," *Journal of Hydrology*, vol. 311, no. 1-4, pp. 134–142, 2005.

[10] J. Erhel, J. R. De Dreuzy, and B. Poirriez, "Flow simulation in three-dimensional discrete fracture networks," *SIAM Journal on Scientific Computing*, vol. 31, no. 4, pp. 2688–2705, 2009.

[11] H. Zhang and J. J. Sheng, "Complex fracture network simulation and optimization in naturally fractured shale reservoir based on modified neural network algorithm," *Journal of Natural Gas Science and Engineering*, vol. 95, article 104232, 2021.

[12] N. Huang, Y. Jiang, R. Liu, B. Li, and S. Sugimoto, "A novel three-dimensional discrete fracture network model for investigating the role of aperture heterogeneity on fluid flow through fractured rock masses," *International Journal of Rock Mechanics and Mining Sciences*, vol. 116, pp. 25–37, 2019.

[13] T. Ishibashi, N. Watanabe, N. Hirano, A. Okamoto, and N. Tsuchiya, "GeoFlow: a novel model simulator for prediction of the 3-D channeling flow in a rock fracture network," *Water Resources Research*, vol. 48, no. 7, 2012.

[14] N. Makedonska, J. D. Hyman, S. Karra, S. L. Painter, C. W. Gable, and H. S. Viswanathan, "Evaluating the effect of internal aperture variability on transport in kilometer scale discrete fracture networks," *Advances in Water Resources*, vol. 94, pp. 486–497, 2016.

[15] C. Yao, Y. Shao, J. Yang et al., "Effects of fracture density, roughness, and percolation of fracture network on heat-flow coupling in hot rock masses with embedded three-dimensional fracture network," *Geothermics*, vol. 87, article 101846, 2020.

[16] Z. Zhao, B. Li, and Y. Jiang, "Effects of fracture surface roughness on macroscopic fluid flow and solute transport in fracture networks," *Rock Mechanics and Rock Engineering*, vol. 47, no. 6, pp. 2279–2286, 2014.

[17] S. R. Brown and C. H. Scholz, "Broad bandwidth study of the topography of natural rock surfaces," *Journal of Geophysical Research: Solid Earth*, vol. 90, no. B14, pp. 12575–12582, 1985.

[18] L. Cheng, G. Rong, J. Yang, and C. Zhou, "Fluid flow through single fractures with directional shear dislocations," *Transport in Porous Media*, vol. 118, no. 2, pp. 301–326, 2017.

[19] W. S. Dershowitz and H. H. Einstein, "Characterizing rock joint geometry with joint system models," *Rock Mechanics and Rock Engineering*, vol. 21, no. 1, pp. 21–51, 1988.

[20] Z. Dou, Z. Chen, Z. Zhou, J. Wang, and Y. Huang, "Influence of eddies on conservative solute transport through a 2D single self- affine fracture," *International Journal of Heat and Mass Transfer*, vol. 121, pp. 597–606, 2018.

[21] Z. Dou, B. Sleep, H. Zhan, Z. Zhou, and J. Wang, "Multiscale roughness influence on conservative solute transport in self-affine fractures," *International Journal of Heat and Mass Transfer*, vol. 133, pp. 606–618, 2019.

[22] G. Grasselli, J. Wirth, and P. Egger, "Quantitative three-dimensional description of a rough surface and parameter evolution with shearing," *International Journal of Rock Mechanics and Mining Sciences*, vol. 39, no. 6, pp. 789–800, 2002.

[23] H. Auradou, G. Drazer, A. Boschan, J. P. Hulin, and J. Koplik, "Flow channeling in a single fracture induced by shear displacement," *Geothermics*, vol. 35, no. 5-6, pp. 576–588, 2006.

[24] D. Crandall, G. Bromhal, and Z. T. Karpyn, "Numerical simulations examining the relationship between wall-roughness and fluid flow in rock fractures," *International Journal of Rock*

Mechanics and Mining Sciences, vol. 47, no. 5, pp. 784–796, 2010.

[25] Z. Dou, S. Tang, X. Zhang et al., "Influence of shear displacement on fluid flow and solute transport in a 3D rough fracture," *Lithosphere*, vol. 2021, no. Special 4, article 1569736, 2021.

[26] N. Watanabe, N. Hirano, and N. Tsuchiya, "Diversity of channeling flow in heterogeneous aperture distribution inferred from integrated experimental-numerical analysis on flow through shear fracture in granite," *Journal of Geophysical Research: Solid Earth*, vol. 114, no. B4, 2009.

[27] Y. Zhang and J. Chai, "Effect of surface morphology on fluid flow in rough fractures: a review," *Journal of Natural Gas Science and Engineering*, vol. 79, p. 103343, 2020.

[28] T. Koyama, B. Li, Y. Jiang, and L. Jing, "Numerical modelling of fluid flow tests in a rock fracture with a special algorithm for contact areas," *Computers and Geotechnics*, vol. 36, no. 1-2, pp. 291–303, 2009.

[29] H. Yasuhara, A. Polak, Y. Mitani, A. S. Grader, P. M. Halleck, and D. Elsworth, "Evolution of fracture permeability through fluid-rock reaction under hydrothermal conditions," *Earth and Planetary Science Letters*, vol. 244, no. 1-2, pp. 186–200, 2006.

[30] N. Huang, R. Liu, and Y. Jiang, "Numerical study of the geometrical and hydraulic characteristics of 3D self- affine rough fractures during shear," *Journal of Natural Gas Science and Engineering*, vol. 45, pp. 127–142, 2017.

[31] Y. Méheust and J. Schmittbuhl, "Flow enhancement of a rough fracture," *Geophysical Research Letters*, vol. 27, no. 18, pp. 2989–2992, 2000.

[32] Y. Méheust and J. Schmittbuhl, "Geometrical heterogeneities and permeability anisotropy of rough fractures," *Journal of Geophysical Research: Solid Earth*, vol. 106, no. B2, pp. 2089–2102, 2001.

[33] S. Murata and T. Saito, "Estimation of tortuosity of fluid flow through a single fracture," *Journal of Canadian Petroleum Technology*, vol. 42, no. 12, 2003.

[34] L. Z. Xie, C. Gao, L. Ren, and C. B. Li, "Numerical investigation of geometrical and hydraulic properties in a single rock fracture during shear displacement with the Navier–Stokes equations," *Environmental Earth Sciences*, vol. 73, no. 11, pp. 7061–7074, 2015.

[35] A. Baghbanan and L. Jing, "Stress effects on permeability in a fractured rock mass with correlated fracture length and aperture," *International Journal of Rock Mechanics and Mining Sciences*, vol. 45, no. 8, pp. 1320–1334, 2008.

[36] H. M. Kim and J. Inoue, "Analytical approach for anisotropic permeability through a single rough rock joint under shear deformation," *Journal of Geophysical Research: Solid Earth*, vol. 108, no. B8, 2003.

[37] B. Li, Y. Jiang, T. Koyama, L. Jing, and Y. Tanabashi, "Experimental study of the hydro-mechanical behavior of rock joints using a parallel-plate model containing contact areas and artificial fractures," *International Journal of Rock Mechanics and Mining Sciences*, vol. 45, no. 3, pp. 362–375, 2008.

[38] V. Rasouli and A. Hosseinian, "Correlations developed for estimation of hydraulic parameters of rough fractures through the simulation of JRC flow channels," *Rock Mechanics and Rock Engineering*, vol. 44, no. 4, pp. 447–461, 2011.

[39] W. Yeo, "Effect of contact obstacles on fluid flow in rock fractures," *Geosciences Journal*, vol. 5, no. 2, pp. 139–143, 2001.

[40] T. Esaki, S. Du, Y. Mitani, K. Ikusada, and L. Jing, "Development of a shear-flow test apparatus and determination of coupled properties for a single rock joint," *International Journal of Rock Mechanics and Mining Sciences*, vol. 36, no. 5, pp. 641–650, 1999.

[41] Q. Feng, J. Jin, S. Zhang, W. Liu, X. Yang, and W. Li, "Study on a damage model and uniaxial compression simulation method of frozen–thawed rock," *Rock Mechanics and Rock Engineering*, vol. 55, no. 1, pp. 187–211, 2022.

[42] H. S. Lee and T. F. Cho, "Hydraulic characteristics of rough fractures in linear flow under normal and shear load," *Rock Mechanics and Rock Engineering*, vol. 35, no. 4, pp. 299–318, 2002.

[43] D. Ma, J. Zhang, H. Duan et al., "Reutilization of gangue wastes in underground backfilling mining: overburden aquifer protection," *Chemosphere*, vol. 264, Part 1, article 128400, 2021.

[44] Y. W. Tsang and P. A. Witherspoon, "Hydromechanical behavior of a deformable rock fracture subject to normal stress," *Journal of Geophysical Research: Solid Earth*, vol. 86, no. B10, pp. 9287–9298, 1981.

[45] J. Zhang, W. B. Standifird, J. C. Roegiers, and Y. Zhang, "Stress-dependent fluid flow and permeability in fractured media: from lab experiments to engineering applications," *Rock Mechanics and Rock Engineering*, vol. 40, no. 1, pp. 3–21, 2007.

[46] Y. Zhang and N. Huang, "Numerical study on the shear-flow behavior and transport process in rough rock fractures," *Comptes Rendus Mécanique*, vol. 346, no. 9, pp. 877–886, 2018.

[47] Z. Zhang and J. Nemcik, "Fluid flow regimes and nonlinear flow characteristics in deformable rock fractures," *Journal of Hydrology*, vol. 477, pp. 139–151, 2013.

[48] C. Zhu, M. C. He, B. Jiang, X. Z. Qin, Q. Yin, and Y. Zhou, "Numerical investigation on the fatigue failure characteristics of water-bearing sandstone under cyclic loading," *Journal of Mountain Science*, vol. 18, no. 12, pp. 3348–3365, 2021.

[49] C. Zhu, M. Karakus, M. He et al., "Volumetric deformation and damage evolution of Tibet interbedded skarn under multistage constant-amplitude-cyclic loading," *International Journal of Rock Mechanics and Mining Sciences*, vol. 152, p. 105066, 2022.

[50] H. Auradou, G. Drazer, J. P. Hulin, and J. Koplik, "Permeability anisotropy induced by the shear displacement of rough fracture walls," *Water Resources Research*, vol. 41, no. 9, article W09423, 2005.

[51] H. Li, Z. Zhong, K. I. I. Eshiet, Y. Sheng, X. Liu, and D. Yang, "Experimental investigation of the permeability and mechanical behaviours of chemically corroded limestone under different unloading conditions," *Rock Mechanics and Rock Engineering*, vol. 53, no. 4, pp. 1587–1603, 2020.

[52] G. Rong, J. Yang, L. Cheng, and C. Zhou, "Laboratory investigation of nonlinear flow characteristics in rough fractures during shear process," *Journal of Hydrology*, vol. 541, pp. 1385–1394, 2016.

[53] X. Xiong, B. Li, Y. Jiang, T. Koyama, and C. Zhang, "Experimental and numerical study of the geometrical and hydraulic characteristics of a single rock fracture during shear," *International Journal of Rock Mechanics and Mining Sciences*, vol. 48, no. 8, pp. 1292–1302, 2011.

[54] N. Barton, S. Bandis, and K. Bakhtar, "Strength, deformation and conductivity coupling of rock joints," *Pergamon*, vol. 22, no. 3, pp. 121–140, 1985.

[55] J. R. de Dreuzy, Y. Méheust, and G. Pichot, "Influence of fracture scale heterogeneity on the flow properties of three-dimensional discrete fracture networks (DFN)," *Journal of Geophysical Research: Solid Earth*, vol. 117, no. B11, 2012.

[56] Y. Jing, R. T. Armstrong, and P. Mostaghimi, "Rough-walled discrete fracture network modelling for coal characterisation," *Fuel*, vol. 191, pp. 442–453, 2017.

[57] Y. Chen, G. Ma, and H. Wang, "Heat extraction mechanism in a geothermal reservoir with rough-walled fracture networks," *International Journal of Heat and Mass Transfer*, vol. 126, pp. 1083–1093, 2018.

[58] J. D. Hyman, M. Dentz, A. Hagberg, and P. K. Kang, "Linking Structural and Transport Properties in Three-Dimensional Fracture Networks," *Journal of Geophysical Research: Solid Earth*, vol. 124, no. 2, pp. 1185–1204, 2019.

[59] T. Ishibashi, N. Watanabe, T. Tamagawa, and N. Tsuchiya, "Three-dimensional channeling flow within subsurface rock fracture networks suggested via fluid flow analysis in the yufutsu fractured oil/gas reservoir," *Journal of Petroleum Science and Engineering*, vol. 178, pp. 838–851, 2019.

[60] R. Liu, B. Li, L. Yu, Y. Jiang, and H. Jing, "A discrete-fracture-network fault model revealing permeability and aperture evolutions of a fault after earthquakes," *International Journal of Rock Mechanics and Mining Sciences*, vol. 107, pp. 19–24, 2018.

[61] P. A. Witherspoon, J. S. Wang, K. Iwai, and J. E. Gale, "Validity of cubic law for fluid flow in a deformable rock fracture," *Water Resources Research*, vol. 16, no. 6, pp. 1016–1024, 1980.

[62] S. R. Brown, "Fluid flow through rock joints: the effect of surface roughness," *Journal of Geophysical Research: Solid Earth*, vol. 92, no. B2, pp. 1337–1347, 1987.

[63] J. Rutqvist, *Coupled Stress-Flow Properties of Rock Joints from Hydraulic Field Testing, [Ph.D. thesis]*, Camborne School of Mines, Cornwall, UK, 1986.

[64] J. Zhao and E. T. Brown, "Hydro-thermo-mechanical properties of joints in the Carnmenellis granite," *Quarterly Journal of Engineering Geology and Hydrogeology*, vol. 25, no. 4, pp. 279–290, 1992.

[65] R. W. Zimmerman and G. S. Bodvarsson, "Hydraulic conductivity of rock fractures," *Transport in Porous Media*, vol. 23, no. 1, pp. 1–30, 1996.

[66] F. Xiong, Q. Jiang, Z. Ye, and X. Zhang, "Nonlinear flow behavior through rough-walled rock fractures: the effect of contact area," *Computers and Geotechnics*, vol. 102, pp. 179–195, 2018.

[67] A. R. Piggott and D. Elsworth, "Analytical models for flow through obstructed domains," *Journal of Geophysical Research: Solid Earth*, vol. 97, no. B2, pp. 2085–2093, 1992.

[68] J. B. Walsh, "Effect of pore pressure and confining pressure on fracture permeability," *Pergamon*, vol. 18, no. 5, pp. 429–435, 1981.

[69] R. W. Zimmerman, D. W. Chen, and N. G. Cook, "The effect of contact area on the permeability of fractures," *Journal of Hydrology*, vol. 139, no. 1-4, pp. 79–96, 1992.

[70] S. Kirkpatrick, "Percolation and conduction," *Reviews of Modern Physics*, vol. 45, no. 4, pp. 574–588, 1973.

[71] Q. Yin, G. Ma, H. Jing et al., "Hydraulic properties of 3D rough-walled fractures during shearing: an experimental study," *Journal of Hydrology*, vol. 555, pp. 169–184, 2017.

[72] A. Baghbanan and L. Jing, "Hydraulic properties of fractured rock masses with correlated fracture length and aperture," *International Journal of Rock Mechanics and Mining Sciences*, vol. 44, no. 5, pp. 704–719, 2007.

[73] J. Long and D. M. Billaux, "From field data to fracture network modeling: an example incorporating spatial structure," *Water Resources Research*, vol. 23, no. 7, pp. 1201–1216, 1987.

[74] P. A. Lapcevic, K. S. Novakowski, and E. A. Sudicky, "The interpretation of a tracer experiment conducted in a single fracture under conditions of natural groundwater flow," *Water Resources Research*, vol. 35, no. 8, pp. 2301–2312, 1999.

[75] C. Masciopinto, "Pumping-well data for conditioning the realization of the fracture aperture field in groundwater flow models," *Journal of Hydrology*, vol. 309, no. 1-4, pp. 210–228, 2005.

[76] N. Huang, Y. Jiang, B. Li, and R. Liu, "A numerical method for simulating fluid flow through 3-D fracture networks," *Journal of Natural Gas Science and Engineering*, vol. 33, pp. 1271–1281, 2016.

[77] Y. W. Tsang, "The effect of tortuosity on fluid flow through a single fracture," *Water Resources Research*, vol. 20, no. 9, pp. 1209–1215, 1984.

[78] J. Gale, R. Mac Leod, and P. LeMessurier, *Site characterization and validation-measurement of flowrate, solute velocities and aperture variation in natural fractures as a function of normal and shear stress, stage 3 (no. STRIPA-TR–90-11)*, Swedish Nuclear Fuel and Waste Management Co., 1990.

[79] H. Jourde, E. A. Flodin, A. Aydin, L. J. Durlofsky, and X. H. Wen, "Computing permeability of fault zones in eolian sandstone from outcrop measurements," *AAPG Bulletin*, vol. 86, no. 7, 2002.

[80] R. Myers and A. Aydin, "The evolution of faults formed by shearing across joint zones in sandstone," *Journal of Structural Geology*, vol. 26, no. 5, pp. 947–966, 2004.